Sizing and Integration of an Electric Propulsion System for a VTOL UAV

Sara de Almeida Pedro
sara.a.pedro@tecnico.ulisboa.pt

Instituto Superior Técnico, Universidade de Lisboa, Portugal

January 2021

Abstract

The advantages of electric vertical take-off and landing (e-VTOL) propulsion systems for military applications have led to the development of unmanned aerial vehicles (UAVs) with this capability. This research presents the propulsion system sizing of four e-VTOL UAVs, assessing the mass, power consumption and installed power for lift-and-cruise and vectored-thrust configurations, intended for a magnetic anomaly detection application.

A study of asymmetric thrust distributions for quadrotors and tri-rotors was performed in order to decrease magnetic interference, concluding that for the defined mission, the use of fewer motors has a higher impact on the total system weight than the efficiency of the configurations, making the vectored-thrust tri-rotor configuration the best performing of all. Regarding efficiency, it was found that sizing the system for VTOL and tilting the rear rotors for forward-flight does not have a negative impact on the required energy for the mission.

Additionally, studies on wing-rotor interference were conducted, determining that, for a required minimum relative net force from the rotors, a minimum distance between surfaces can be calculated knowing the percentage of rotor covered area.

The methods applied for propulsion sizing include vortex theory and Corke's empirical method, while CFD studies were completed to determine wing-rotor interference. The estimated performance of the configurations was then compared with their experimental performance through static tests, rendering similar results.

Finally, a dynamic model was developed, confirming the configurations were stable and controllable, prior to an indoor hover test of the manufactured UAV.

Keywords: e-VTOL, electric propulsion, UAV, wing-rotor interference

1. Introduction

The pressure from resource scarcity and environmental concerns on the industry of today has resulted in alternative propulsion systems garnering renovatedattentio[1]. Electrically-propelled, high-efficiency vehicles offer an answer to this paradigm shift [2].

This fundamental change has made UAVs an attractive investment, resulting in numerous developments in the area. Military grade surveillance is one of the new purposes that rose from such innovations, taking advantage of the low heat and noise signatures that e-VTOL provides. As a result, the focal point of these vehicles becomes the propulsion system, leading to an important investigative work on different propulsion architectures and configurations [3].

For that purpose, this research presents the propulsion system sizing for VTOL and forward-flight of four scaled down prototype UAVs aimed at military detection through magnetic signature, comparing them against each other to determine which best fits the mission. These four prototypes share a similar structure, differing mostly in propulsion architecture. Configuration one adds a VTOL system to the previous UAVs developed for the mission, featuring a pusher to complete the lift-and-cruise architecture; comparatively, configuration two has the same architecture, but an asymmetric thrust distribution, with the rear rotors producing 80% of the thrust required during VTOL. On the other hand, configuration three has the same VTOL system of configuration two, but has a vectored-thrust architecture, tilting the rear rotors for forward flight. This configuration also features retractable front rotors to have a higher L/D during cruise condition. Finally, configuration four has the same features as configuration three - retractable booms, tilting rear rotor-, but based on a tri-rotor VTOL system instead of a quadrotor.

The propulsion systems were sized by use of a vortex theory model, as well as through the available experimental data, validating the model by comparing its results to static tests. Their mass, efficiency and power consumption was assessed, taking into consideration the penalties that surface from partially covered rotors through both CFD (computational fluid dynamics) simulations and static thrust experimental tests. Additionally, a dynamic model was developed, confirming that all the developed configurations were stable and controllable, prior to performing hover flight tests.

2. Literature Review

The history of unmanned aerial vehicles (UAVs) dates back to WWI, to gather and transmit real-time information from hostile areas without endangering aircrew. However, it would not be until the state of the art progressed in automatic stabilisation, remote-control, and autonomous navigation that UAVs would become a viable alternative to manned aircraft [4].

With the evolution of UAVs, e-VTOL capability became one of the most common features, as it combines the negligible variation in efficiency at different dimensions of electric motors with the ability to take-off without a runway, performing efficiently in both lift-and-cruise and vectored-thrust configurations [5].

In electrically-propelled UAVs [6], the sizing of the motor depends on the mission and configuration, as the required thrust-to-weight ratio per motor will dramatically increase with manoeuvres. Since take-off is the most demanding flight stage, requiring the highest thrust-to-weight ratio, it dictates the motor selection in vectored thrust configurations. However, motors for lift-and cruise configurations can be sized according to the flight stage they perform.

On the other hand, propeller choice hinges on design priority, as performance and efficiency can be traded for stealth or even compliance with a specific motor. Assuming a design to maximise thrust output while maintaining a power consumption compatible with the chosen motor around a specific design point, parameters such as thrust and power coefficients, in addition to efficiency, indicate performance [7].

For a fixed-pitch propeller design can be accomplished through optimised methods going from blade element methods, passing by vortex methods, to numerical ones. The simplest axial momentum theory models the rotor as an infinitely thin, finite in area actuator disc, disregarding blade geometry; that makes blade element methods more accurate, yet still dependent on correction factors originated in blade element momentum methods (BEM)[8][9], the most accurate of the above mentioned. Vortex theory is another valid approach, built on Betz's principle by Goldstein and continued by Theodorsen and Larrabee [10] [11].

An alternative to these studies is applying computational fluid dynamics (CFD) software. Currently, CFD software is used to determine propeller behaviour and assess performance by solving the Reynolds-Averaged Navier-Stokes (RANS) equations [12], allowing the study of more complex problems and flow conditions, such as the interaction between rotor and wing [13][14].

3. Propulsion Sizing

The use of propeller momentum theory has allowed the parametric study of power consumption as a function of rotor positioning and thrust-overweight (T/W) ratio by applying equation 1.

$$P_i = T_i V_c - \frac{k_i}{2} T_i V_c + \frac{k_i T_i}{2} \sqrt{{V_c}^2 + \frac{2T_i}{\rho A_i}} + \frac{\sigma C_{d0}}{8} \rho A_i {V_{tip}}^3 \quad (1)$$

As a result, it was proven that power consumption hinges only on T/W ratio for the same total disc area. This conclusion determined the position of the rotors of the asymmetrically distributed propulsion systems to a ratio of 20% to 80%, while keeping the T/W ratio at the minimum required - 1.3.

3.1. Requirements

The mission requirements that determined the propulsion selection were established by the project managers in compliance with the requests from the commissioning entities. These are presented below in table 1.

Requirement	Description
Minimum T/W_{max}	1.3
T/W_{Climb}	1.05
Cruise speed	20 m/s
D_{pusher} propeller	15 in
D_{max} propeller	15 in (quadrotors)
Single battery	6S - 22.2V (quadrotors)

Table 1: Propulsion requirements

Additionally, the propulsion system must be able to perform the defined mission, requiring a battery capable of providing 60 seconds of power for take-off, 30 seconds of power for landing, 10 seconds of power at maximum throttle, 20 minutes of cruise time and a 20% backup. Using these requirements the selection of the propulsive components took place, validating the results with a vortex theory model as well as available experimental data for each configuration.

3.2. VTOL system selection and validation

Following the aforementioned requirements the selection of the VTOL system was conducted, using highest efficiency and lowest component mass as criteria. The selected combinations of motor and propeller resulted from a survey of the available options and are presented on table 2 below.

Configuration	Front Rotor	Rear Rotor
Configuration 1	MN4012	MN4012
Motor & propeller	14x4.8	14x4.8
Configuration 2	MN3110	MN5212
Motor & propeller	11x3.7	15x5
Configuration 3	MN3110	MN5212
Motor & propeller	11x3.7	15x5
Configuration 4	MN3110	P60
Motor & propeller	11x3.7	22x6.6

Table 2: Selected VTOL components

The electric speed controllers (ESCs) where chosen according to manufacturer advice, ensuring compatibility in both current and voltage. The validation of the chosen combinations was performed with a vortex theory model, yielding the results on table 3.

Propeller D[in]xP[in]	Thrust Difference [%]
11x3.7	13.23
14x4.8	13.8
15x5	13.6
22x6.6	13.52

Table 3: VTOL thrust validation

The discrepancy between the experimental and theoretical values is between 13% and 14%, resulting from approximations made for unknown parameters of the propeller geometry, as well as from assumptions from the vortex theory's model itself. Despite the difference in results, the choice was validated for purchasing.

Unfortunately, the 11x3.7 propeller was no longer available at the time of purchasing, and a 12x4 was purchased in its place.

3.3. Forward-flight System Selection and Validation

The method for the motor-propeller selection for forward-flight is similar to the VTOL process, basing the choice on required power rather than static thrust. Corke's propeller design method was used to compute the required power, as shown by equation 2.

$$P = \frac{TV}{\eta_p} = \frac{WV}{\frac{L}{D}\eta_p} \tag{2}$$

The L/D in cruise of each configuration was estimated through Ansys® simulations, yielding 16.44, 13.91, 18.55 and 19.34 for configurations one to four, respectively.

Knowing the L/D, as well as the cruise speed, experimental data from propellers was entered into a developed MATLAB® script to compute power, efficiency and RPM through interpolation. The chosen propeller - APC 15x13N - for the pusher of the lift-and-cruise configurations is shown on table 4, as well as its specifications.

	Efficiency [%]	Power [W]	Rotation RPM
Configuration 1	80.68	103.37	3434.6
Configuration 2	83.31	118.12	3621

Table 4: Estimated propeller performance

The pusher motor was chosen based on voltage compatibility and lowest mass, while ensuring sufficient power and RPM to meet the propeller's requirements - KDE 4012 KV400. The ESC was selected based on the previously mentioned criteria.

Prior to purchasing, the selected pusher components were validated with the mentioned vortex theory model and the tilting rotor's performance in cruise was evaluated, ensuring mission performance. The results can be seen in table 5.

	Power [W]	Efficiency [%]
Configuration 1	95	87.79
Configuration 2	114.16	86.54
Configuration 3	92.02	80.42
Configuration 4	92.64	76.64

Table 5: Power and efficiency for cruise

The power estimated for cruise condition with the vortex theory model is 8% and 3.5% lower for configurations one and two, respectively, than the one estimated from propeller curves, thus validating the choice for purchasing.

3.4. Power Distribution and Consumption

Having the components selected, available power was calculated, as seen on table 6, comparing all four configurations.

Configuration	1	2	3	4
Installed power [W]	3285.6	4040.4	3330	2490
Forward-flight [%]	21	18	80	73
Front rotors [%]	50	20	20	27
Rear rotors [%]	50	80	80	73

Table 6: Power distribution

Configuration four presents the least installed power due to having fewer motors, whereas configuration two shows the highest installed power,

as well as the lowest available for forward-flight. Both vectored-thrust configurations have significantly higher power available for forward-flight due to tilting the rear rotors to perform this flight condition.
In hover, configurations one through three show similar results, with a difference under 3% between them, while configuration four has the least power demands, consuming over 8% less.
In cruise, configuration two has a penalty of 20% increase in power consumption when compared to configuration one, whereas configurations three and four reveal benefits under 5%, neutralising the lower efficiency of the propellers, as seen in table 7.

Power/Configuration	1	2	3	4
Hover [W]	1089.28	1119.6	1119.6	997.52
Hover [%]	100	102.8	102.8	91.6
Cruise [W]	95	114.16	92.02	92.64
Cruise [%]	100	120.3	96.9	97.5

Table 7: Power consumption per flight condition

3.5. Mass and Battery Estimation

Having selected the components and estimated their power consumption in the different flight conditions, the battery mass and the overall mass of the system could be computed, as seen in table 8.

Configuration	1	2	3	4
Energy [Wh]	77.91	81.27	72.42	75.29
Battery mass [Kg]	0.46	0.48	0.43	0.44
Component mass [Kg]	1.115	1.238	0.924	0.7595
Total mass [Kg]	1.57	1.72	1.35	1.20
Mass difference [%]	0	9.08	-14.20	-23.59

Table 8: Energy consumption and system's mass

The energy required for the mission was calculated with the power required for each mission segment as well as its duration, using the energy density of the battery chosen for the mission - 170.33 Wh/Kg. As expected, configurations three and four have a lighter propulsion system, given that they feature fewer components. When it comes to energy demands, configuration three has the least required energy due to a more efficient cruise condition - the longest mission segment. For this particular mission, both vectored-thrust configurations perform better than their lift-and-cruise competitors, having a lighter and more energy-efficient propulsion system.
If the penalties in mass of configuration two or the benefits of configurations three and four were applied as battery, the duration of each mission segment would change. This variation is presented on table 9.

Variation /Configuration	2	3	4
Take-off time [s]	-21.54	37.81	60.42
Landing time [s]	-10.77	18.9	30.21
Max throttle time [s]	-3.59	6.30	10.07
Endurance [s]	-430.8	756.12	1208.35
Range [Km]	-4.62	15.12	24.17

Table 9: Range Variation with Battery Distribution

With this battery distribution, configuration two maintains the ability to perform take-off at the desired vertical climb velocity, making landing the most problematic mission segment. As for the two other configurations, there is a significant increase in time - or power - allocated for each mission segment, with an increase of over 60% relative to the initial range for configuration three, and reaching double the range for configuration four.

3.6. Rotor Coverage

In order to compute the net force loss of configurations two through four due to partially covered rotors, CFD studies were performed for different relative distances and covered areas. For each case, various simulations were conducted, increasing the number of elements of the mesh until the results converged. Figures 1 and 2 present the results obtained.

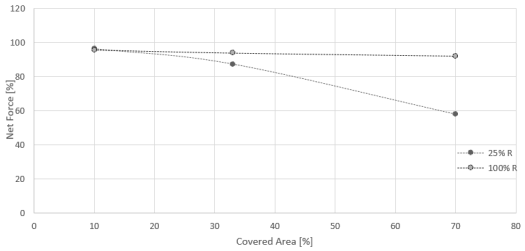

Figure 1: Thrust variation with covered area

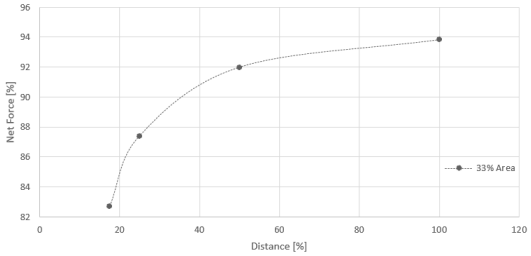

Figure 2: Thrust variation with distance

These estimations, as well as the percentage of covered area of the rotors, made it possible to compute a minimum distance between surfaces, as presented on table 10.

Rear Rotors/Configuration	2 & 3	4
Covered Area [%]	69	63
Available Thrust [N]	40.96	79.60
Required Thrust [%]	87.18	89.72
Required distance [%]	88.75	92.82
Required distance [m]	0.169	0.259

Table 10: Required rotor-wing distance

This data was validated with experimental static tests to obtain the minimum required distance at which the rotors must be placed from the wing.

4. Static Experimental Tests

The power, mass and battery estimations of the previous section were compared against results the from static test bench. To do so, a setup comprised of a motor mount, a power box, a power source, a data acquisition system, and an emergency stop button were used, testing each motor-propeller-ESC combination.

4.1. Thrust vs Throttle

The thrust vs throttle curves follow the expected quadratic tendency, producing significantly more thrust than expected. Table 11 presents the throttle at which each VTOL motors performs a given mission segment.

Configuration	1	2 & 3	
Throttle	All Rotors	Front Rotors	Rear Rotors
Take-off [%]	73.94	51.15	82.20
Hover [%]	71.55	53.04	80.02
Landing [%]	69.08	51.15	77.71
T/W_{Max}	1.70	2.57	1.51

Table 11: Throttle and T/W comparison

All rotors respect the required T/W ratio; configuration one performed VTOL with a 70%-75% throttle, having an available T/W ratio of 1.7. On the other hand, configuration two is significantly oversized, especially regarding the front rotors. The unavailability of the chosen propellers hinders efficiency since the motors will only be used at around 50% throttle. However, the rotors are partially covered and the tests were performed at a higher voltage - fully charged battery rather than nominal voltage -, which means experimental results for rotor coverage and potential hover tests should determine whether the chosen propulsion system is oversized.

4.2. Thrust vs Power

Regardless of the differences between the model and the experimental procedure, the results of the static test are very close to the ones from the vortex theory model for all three ESC-motor-propeller combinations, validating the previous use of the model to estimate performance in static cases. Table 12 presents the relative differences between the two results for the thrust obtained at 100% throttle, where the error goes up to 5.18%.

Configuration	1	Configuration 2 & 3	
	All Rotors	Front Rotors	Rear Rotors
Thrust [N]	29.23	17.61	41.12
Test Power [W]	498.92	270.48	725.50
Model Power [W]	477.97	256.46	732.17
Difference [%]	4.20	5.18	0.92

Table 12: VTOL results

Regarding the power consumption, configurations two and three consume slightly more power at every flight stage. However, the 1% difference is a small penalty when compared to the advantages of having an asymmetric thrust distribution. Additionally, the data corroborated the initial assumption that power consumption for a given T/W ratio and total disc area doesn't significantly change with rotor position [1].

4.3. Experimental Mass and Energy

Taking into account the power required for the different VTOL mission segments, a new estimation for battery mass can be performed to obtain a more accurate prediction of the mass of the propulsion system. Table 13 presents these results where the estimations for cruise power presented in the previous chapter were used [2].

Configuration	1	2	3
Total Energy [Wh]	73.42	81.55	72.69
Total Energy [%]	100	111.07	99.01
Battery Mass [Kg]	0.431	0.479	0.427
Total Mass [Kg]	1.546	1.717	1.351
Total Mass [%]	100	111.06	87.39

Table 13: VTOL system's mass - uncovered

When compared to the estimations performed previously, the same tendency is observed and the total system mass of the different configurations does not change significantly, confirming the accuracy of the initial predictions.

Evaluating the configurations relative to each other, configuration three has the least energy demands and component mass, resulting in a significantly lighter propulsion system. While having the same VTOL system as configuration three, configuration two has a severe penalty in power consumption during cruise condition, due to a lower $\frac{L}{D}$, as well

[1] The total disc area of configurations two and three is 94% relative to the disc area of configuration one.

[2] The relative results use configuration one as reference

as a heavier component mass, featuring one extra rotor that results in a significant propulsion system mass difference.

4.4. Experimental Rotor Coverage

To estimate the actual thrust output decrease due to wing-rotor interference and calculate the minimum distance between surfaces to fulfil project requirements, an experimental procedure was performed partially covering the rotors.

The procedure used the test bench setup as well as a system of rods with a wooden plate connected to the motor mount, allowing tests to be performed with several distances and covered areas.

The tests were performed on the chosen motor, for reference, and then with the supporting structure prior to adding the wooden plate, keeping a constant voltage source to ease comparison. The results for the tested areas and distances are presented on figures 3 and 4.

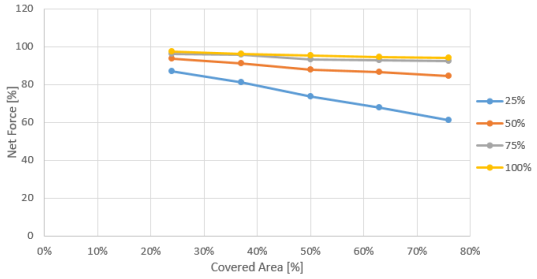

Figure 3: Experimental thrust variation with covered area

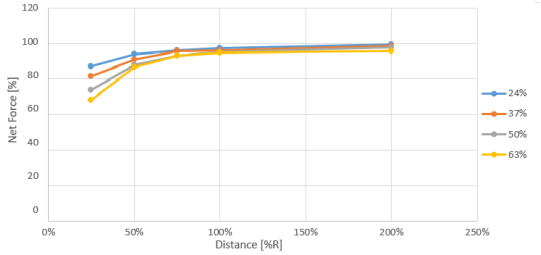

Figure 4: Experimental thrust variation with covered distance

In Figure 3, the predicted behaviour of thrust with the covered area is confirmed. Figure 4 also validates the tendency estimated with computational simulations, confirming the asymptotic behaviour of the net force with distance for all covered areas. As expected, the variation in net force is more significant for the cases with more covered area, decreasing 12.5% with coverage of 24% and 28% for a covered area of 63% across the same relative distance variation.

When comparing the results to the ones obtained through CFD simulations, figure 5 presents the same linear tendency for both data sets.

On the other hand, figure 6 shows larger discrepancies between computational and experimental

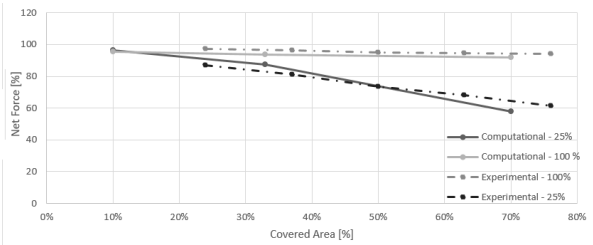

Figure 5: Computational vs experimental data variation with covered area

results. Given that the comparison is not done for the same covered area - 33% computational and 37% experimental - some differences were expected. Additionally, the data gathered from computational simulations were obtained with a 23" propeller with significantly different characteristics from the 15" propeller used experimentally. Regardless of the differences in the studies, both data curves show the beginning of an asymptotic behaviour at 100% relative distance as well as an increase in net force with distance.

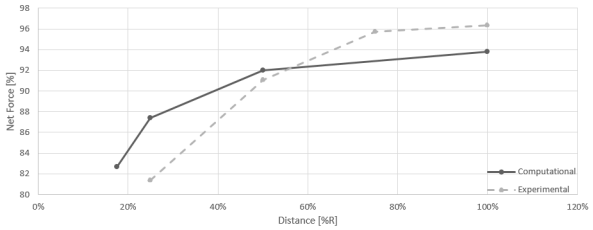

Figure 6: Computational vs experimental data variation with distance

With this data, the required distance between surfaces was calculated and compared with the CFD results. Table 14 shows these results where the error between computational and experimental data was linearized due to lack of points.

Rear Rotors	Configurations 2 & 3	Configuration 4
Available T/W	1.5	1.45
Required Thrust [%]	86.66	89.66
Required distance - Computational [%]	66.19	65.76
Required distance - Experimental [%]	53.75	51.22

Table 14: Experimental and computational required rotor-wing distance

The discrepancy between results is significant, but somewhat expected given the use of different types of propellers and conditions for the simulations and the experiments.

Table 15 shows the system's mass and energy requirements for a distance of 75% between surfaces. Comparing it to the uncovered situation, both configurations feature around 1% total mass increase, since the variation in required energy is about 4.5%. With insufficient data provided from the manufacturers to relate throttle to thrust and estimate power consumption for the covered rear ro-

Configuration	1	2	3
Total Energy [Wh]	73.42	84.8	75.96
Battery Mass [Kg]	0.431	0.498	0.446
Total Mass [Kg]	1.546	1.736	1.370
Total Mass [%]	100	112.3	88.6

Table 15: VTOL system's mass - covered

tor of configuration four, its battery penalties were not computed.

5. Flight Dynamics Model

In order to ensure that the designed configurations were stable and controllable, a dynamics model was derived for the VTOL - multicopter - mode. This model assumes the UAV is a rigid-body, accounting for thrust, torque and some aerodynamic effects of the wing, canard and fuselage structures. The dynamics of the UAV can be separated into two major contributors - aerodynamic and propulsive - as seen below [15].

$$\begin{bmatrix} F \\ M \end{bmatrix} = \begin{bmatrix} F_a \\ M_a \end{bmatrix} \Delta X + \begin{bmatrix} F_p \\ M_p \end{bmatrix} \Delta U \tag{3}$$

Where X is the state vector and U is the actuation vector. The propulsive components of force and moments can be accounted for as a function of propeller rotational speed. Equations 4 and 5 translate this relation.

$$T_i = K_{T_i} {\Omega_{p_i}}^2 \tag{4}$$

$$\tau_i = K_{\tau_i} {\Omega_{p_i}}^2 \tag{5}$$

With this relation as well as the data presented on figure 7, the linearised - for hover condition - propulsive forces and moments can be calculated.

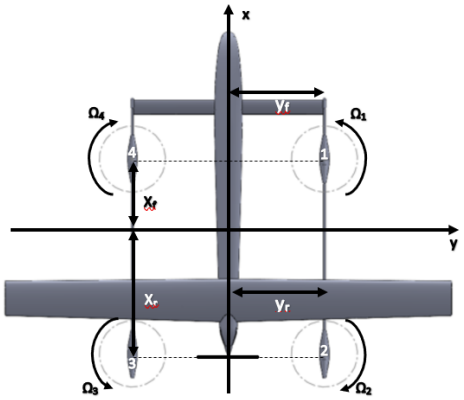

Figure 7: Reference frame

$$\begin{cases} \Delta F_{z_p} = -2(K_{T_1}\Omega_{0_1}\Delta\Omega_1 + K_{T_2}\Omega_{0_2}\Delta\Omega_2 + K_{T_3}\Omega_{0_3}\Delta\Omega_3 + K_{T_4}\Omega_{0_4}\Delta\Omega_4) \\ \Delta M_{x_p} = 2y_f(K_{T_4}\Omega_{0_4}\Delta\Omega_4 - K_{T_1}\Omega_{0_1}\Delta\Omega_1) + 2y_r(K_{T_3}\Omega_{0_3}\Delta\Omega_3 - K_{T_2}\Omega_{0_2}\Delta\Omega_2) \\ \Delta M_{y_p} = 2x_f(K_{T_1}\Omega_{0_1}\Delta\Omega_1 + K_{T_4}\Omega_{0_4}\Delta\Omega_4) - 2x_r(K_{T_3}\Omega_{0_3}\Delta\Omega_3 + K_{T_2}\Omega_{0_2}\Delta\Omega_2) \\ \Delta M_{z_p} = -2K_{\tau_1}\Omega_{0_1}\Delta\Omega_1 + 2K_{\tau_2}\Omega_{02}\Delta\Omega_2 - 2K_{\tau_3}\Omega_{0_3}\Delta\Omega_3 + 2K_{\tau_4}\Omega_{0_4}\Delta\Omega_4 \end{cases} \tag{6}$$

The aerodynamic components can be computed in a similar fashion. However, since the trim state is hover, all the linearised components of the aerodynamic forces are zero, and the non-linear terms must be used instead.
The system of equations below presents these components.

$$\begin{cases} F_{x_a} = -\frac{1}{2}\rho C_{d_0} S_w \Delta u^2 \\ F_{y_a} = -\frac{1}{2}\rho C_{D_f} S_f \Delta v^2 \\ F_{z_a} = -\frac{1}{2}\rho(C_{d_w}(S_w + S_c) + 0.5 C_{d_f} S_f)\Delta w^2 \\ M_{x_a} = 0 \\ M_{y_a} = -\frac{1}{2}\rho(C_{D_w}(S_w d_w + S_c d_c) + C_{D_f}\frac{S_f}{2} d_f)\Delta w^2 \\ M_{z_a} = -\frac{1}{2}\rho C_{d_f}\frac{S_f}{2} d_f \Delta v^2 \end{cases} \tag{7}$$

As for the longitudinal direction, the forces were calculated in the usual manner, using the zero angle of attack drag coefficient. The lateral force was assumed to be the fuselage drag in this direction, as it is the main contributor. Finally, the force in the vertical direction was estimated to be the drag of the wing, canard and fuselage. Without the actual drag coefficient of the different surfaces, the drag coefficient of the fuselage was approximated to the drag coefficient of a cylinder, while the wing and canard's were approximated to the drag coefficient of a flat plate.

5.1. Simulink Model

The mathematical model was used to derive a Simulink Model simulating the behaviour of the UAV. The model is run through a MATLAB® script, where the *trim* function is called. This function computes the hover propeller rotation for a given choice of configuration, knowing the motor's thrust and torque constants, as well as the UAV's mass and inertia. It outputs the reference state vector, xref. This vector is subtracted from the current state to obtain Δx, that goes into the function *dof*, together with the actuator vector Δu. The variation in forces and moments is then calculated in this function, through the derived flight dynamics model, and input them into an aerodynamics block that calculates a new state.
The new state is entered into the control section where, through PID controllers, a new signal is defined and fed into the *gains* function [16]. A mixer matrix in this function transforms the PID signals into the new rotor actuation. The mixer is presented below.

$$\begin{bmatrix} \frac{-2K_{T_1}\Omega_{0_1}}{m} & \frac{-2K_{T_2}\Omega_{0_2}}{m} & \frac{-2K_{T_3}\Omega_{0_3}}{m} & \frac{-2K_{T_4}\Omega_{0_4}}{m} \\ -2\Omega_{0_1}\frac{I_{zz}K_{T_1}+I_{xz}K_{T_1}y_f}{I_{xx}I_{zz}-I_{xz}^2} & 2\Omega_{0_2}\frac{I_{zz}K_{T_2}-I_{xz}K_{T_2}y_r}{I_{xx}I_{zz}-I_{xz}^2} & 2\Omega_{0_3}\frac{-I_{zz}K_{T_3}+I_{xz}K_{T_3}y_r}{I_{xx}I_{zz}-I_{xz}^2} & 2\Omega_{0_4}\frac{I_{zz}K_{T_4}+I_{xz}K_{T_4}y_f}{I_{xx}I_{zz}-I_{xz}^2} \\ \frac{2x_f K_{T_1}\Omega_{0_1}}{I_{yy}} & \frac{-2x_r K_{T_2}\Omega_{0_2}}{I_{yy}} & \frac{-2x_r K_{T_3}\Omega_{0_3}}{I_{yy}} & \frac{2x_f K_{T_4}\Omega_{0_4}}{I_{yy}} \\ -2\Omega_{0_1}\frac{I_{xx}K_{T_1}+I_{xz}K_{T_1}y_f}{I_{xx}I_{zz}-I_{xz}^2} & 2\Omega_{0_2}\frac{I_{xx}K_{T_2}-I_{xz}K_{T_2}y_r}{I_{xx}I_{zz}-I_{xz}^2} & 2\Omega_{0_3}\frac{-I_{xx}K_{T_3}+I_{xz}K_{T_3}y_r}{I_{xx}I_{zz}-I_{xz}^2} & 2\Omega_{0_4}\frac{I_{xx}K_{T_4}+I_{xz}K_{T_4}y_f}{I_{xx}I_{zz}-I_{xz}^2} \end{bmatrix} \tag{8}$$

After properly tuning the controller and stabilising the different variables, the stabilisation time and rates could be estimated for each of them.

5.2. Model Results

The Simulink model was adjusted, allowing the study of the dynamics of configuration one as well as configurations two and three; this was done assuming the latter two feature the same inertia, motor saturation and drag coefficients.

Comparing the same request in altitude, all configurations reach the request at approximately the same time, requiring the same rate in vertical velocity as seen in figures 8 and 9. Nevertheless, the rates achieved in pitch are more accentuated for configurations two and three due to having lower inertia values.

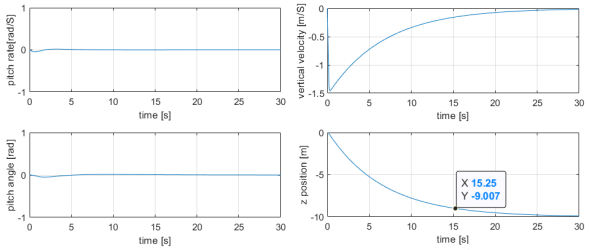

Figure 8: Configuration 1 - -10 m altitude

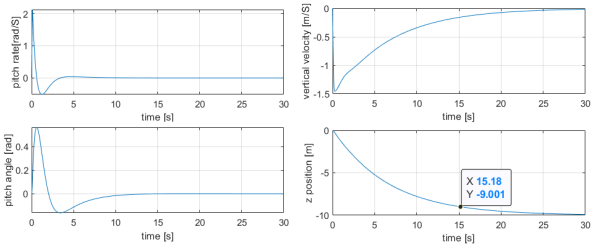

Figure 9: Configuration 2 & 3 - -10m altitude

Evaluating the behaviour from a request of 10º in pitch, both configurations show the same type of response, reaching the request at the same time and exhibiting the same rate while maintaining a constant position.

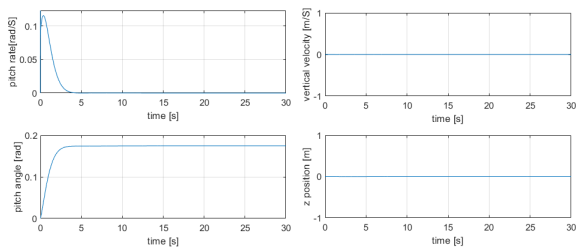

Figure 10: Configuration 1 - 10º pitch

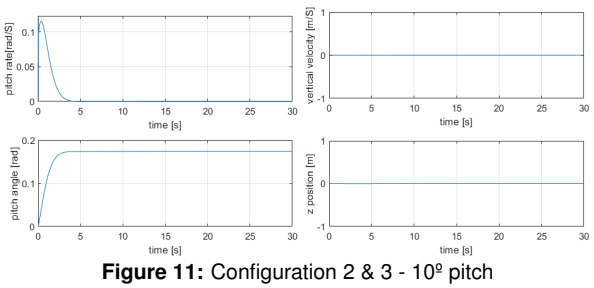

Figure 11: Configuration 2 & 3 - 10º pitch

Figures 12 and 13 present the response of the UAVs to a request of 1º in roll. The lower roll request is a consequence of the instability the model presents for roll angles over 3º. As the roll motion is input into the system, lateral velocity surfaces, which increases the aerodynamic yaw moment to a point at which the torque of the motors cannot balance, thus creating instabilities. From here, two possible solutions present themselves: either the lateral aerodynamic force is overestimated, therefore producing an overly large moment, or the model can't produce roll motion, requiring motors with higher torque constant and KV to balance the generated yaw moment.

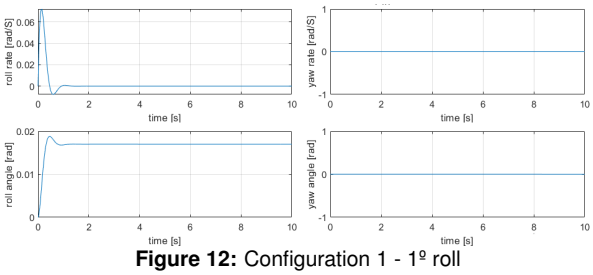

Figure 12: Configuration 1 - 1º roll

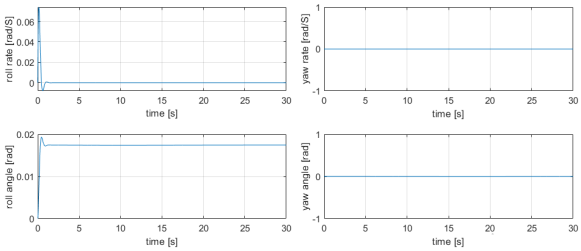

Figure 13: Configuration 2 & 3 - 1º roll

To complete the analysis of the modelled variables, figures 14 and 15 present the curves resultant from a 10º yaw request.

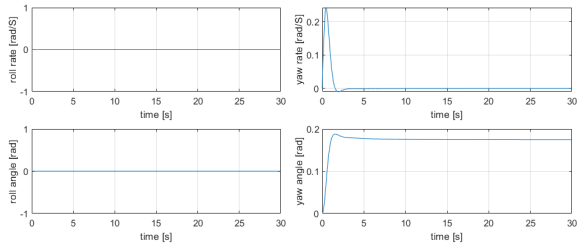

Figure 14: Configuration 1 - 10º yaw

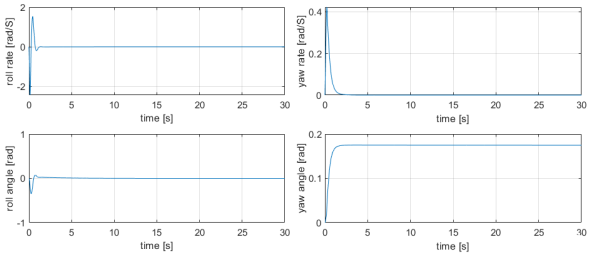

Figure 15: Configuration 2 & 3 - 10º yaw

Although the stabilisation time is somewhat similar for both configurations, the required rate to achieve

it is significantly different, with over 0.2 for configuration one, but 0.4 for configurations two and three. Additionally, there is an oscillation in roll for the latter configurations as a consequence of an inertia value that is close to half of the one calculated for configuration one.
While the results between configurations might differ, the model predicts the UAV to be stable and controllable, adding an extra security layer to the hover tests.

6. Hover Test

Having manufactured, assembled and integrated the scalded down prototype corresponding to configuration one, static load tests were performed in key structural components, the avionics systems were tested and the controller was tuned through flight tests of UAVs with the same system. With every commissioning test performed, indoor hover tests were carried out, as fixed-wing flights would require the tests to be held outside, which meant adding administrative work that could not be completed within the given time frame.
Figure 16 presents the fully assembled and instrumented UAV at the test site.

Figure 16: Configuration One

6.1. Flight Tests

In order to ensure safety of the crew, the first test performed was a hover test, confirming all rotors are rotating in the correct direction, that the centre of gravity is placed at the design position and that there are no severe structural oscillations. This flight lasted 30 seconds and yielded positive results, allowing the remaining tests to be performed. The second flight test proceeded with the goal of ensuring proper tuning of the controller with small inputs in roll, pitch and yaw. These tests were followed by tests where doublets were commanded into the UAV in the three directions to observe its response to disturbances.

6.2. Hover Power Consumption

The two last tests were used to assess the UAV's performance, since they had a longer duration that resulted in an abundance of data to analyze during hover condition. However, the avionics part that had been responsible for recording the power allocated to each motor malfunctioned and had to be removed. Lacking this device, the power consumption of each motor was unknown and had to be estimated from battery consumption. Table 16 shows the battery consumed by the motors during each flight

Energy Consumption Flight Test	Battery [Ah]	Avionics [Ah]	Motor [Ah]	Duration [s]
1	5.29	0.21	5.08	382
2	6.96	0.7	6.26	466

Table 16: Flight Test Power Consumption

Knowing the total capacity consumed by the motors and the duration of the flight, the average current given to each motor can be calculated as presented below.

$$\Rightarrow Motor\ \ Current = \frac{Capacity\ \ Consumption}{4 \times Flight\ \ Duration}$$

The average current was then multiplied by the average voltage per test to calculate the power consumption for each flight test.

Flight Test	Current [A]	Voltage [V]	Power [W]	Total Power [W]
1	11.97	23.81	285.0	1140.0
2	12.09	23.73	286.9	1147.6

Table 17: Hover Performance

Compared to the results obtained in the static test bench, these values are significantly higher than expected, exceeding estimations in 21.7% and 22.5% for flights one and two, respectively. While significant, the discrepancy can be explained by an accumulation of errors, such as manoeuvres performed during flight, the usage of an average current, significant ground effect and structural bending.

7. Conclusions

The development of this research entailed the sizing of the VTOL and forward-flight propulsion system of four different configurations, comparing each of their performances against each other. To do so, efficiency, mass and power consumption were evaluated with vortex theory models, as well as static thrust tests, on the purchased components. Additionally, CFD simulations were performed to quantify wing-rotor interference, and compared to the data obtained from experiments conducted to that end. Finally, a flight dynamics model was derived, ensuring the manufactured configuration was stable and controllable prior to an indoor hover test, which represents the most significant achievement of this research thus far.
As evidenced in this document, the initial set of objectives has been met: from sizing the propulsion

system of all four configurations, to confirming that the target configuration better performs the stated mission in almost every metric.

With regard to the used models, the vortex theory model has been validated with marginal errors when compared to experimental tests. The CFD simulations on rotor coverage were similarly validated against experimental data confirming the asymptotic tendency of the net force curve as a function of the relative distance between surfaces. Furthermore, the experimental tests on rotor coverage can set a standard for determining the minimum relative distance between rotor and wing for a given covered area. Other accomplishments include the development of a flight dynamics model, tuning the controller to respond correctly to step inputs in all its rates for all the quadrotor configurations.

7.1. Future Work

First and foremost, this research lacks the experimental evaluation of the chosen forward-flight propulsion system. As mentioned before, there are complicated steps that must be taken in order to fly a UAV outdoors in Canada, which is required to test the pusher rotor in fixed-wing mode. While the bureaucratic procedures could not be completed within the time frame of this thesis, the UAV is ready to fly, and given permission from TA, the performance of the pusher rotor can be ascertained.

Secondly, the evaluation of the magnetic signature of the VTOL system as compared to the previous configurations should take place, guaranteeing that it does not compromise the purpose of the UAV. This step can take place as soon as the Qu-spin magnetic sensor is available, as the UAV was manufactured already accounting for its mass and volume.

The quantification of the magnetic interference of the VTOL system of configuration one should be followed by the development of the remaining configurations, evaluating their performance and comparing them with that of the base configuration. This will confirm the conclusions presented so far, supporting that the vectored-thrust tri-rotor configuration is the best one for the chosen mission.

The fourth step requires the continuity of the project into the future, extending the partnership between the institutions to develop the full scale propulsion system. Since the full scale prototype weighs 25 kg, investigation into other types of propulsion while maintaining the defined architecture should be seriously considered.

References

[1] J. Lieh, E. Spahr, A. Behbahani, and J. Hoying, "Design of Hybrid Propulsion Systems for Unmanned Aerial Vehicles," July 2011.

[2] Mohamed Nadir Boukoberine, Zhibin Zhou, and Mohamed Benbouzid, "A Critical Review on Unmanned Aerial Vehicles Power Supply and Energy Management: Solutions, Strategies, and Prospects," vol. 255, Dec. 2019.

[3] M. Jaeger and D. Adair, "Conceptual Design of a High-Endurance Hybrid Electric Unmanned Aerial Vehicle," Aug. 2016.

[4] J. Keane and S. Carr, "A Brief History of Early Unmanned Aircraft," *Johns Hopkins Apl Technical Digest*, vol. 32, pp. 558–571, Dec. 2013.

[5] A. Bacchini and E. Cestino, "Electric VTOL Configurations Comparison," *Aerospace*, vol. 6, p. 26, Mar. 2019.

[6] B. Bilgin, J. Liang, M. Terzic, J. Dong, R. Rodriguez, E. Trickett, and A. Emadi, "Modeling and Analysis of Electric Motors: State-of-the-Art Review," *IEEE Transactions on Transportation Electrification*, vol. PP, pp. 1–1, July 2019.

[7] G. Kuiper, "New developments and propeller design," *Journal of Hydrodynamics, Ser. B*, vol. 22, pp. 7–16, Oct. 2010.

[8] R. MacNeill and D. Verstraete, "Blade element momentum theory extended to model low Reynolds number propeller performance," *The Aeronautical Journal*, vol. 121, no. 1240, pp. 835–857, 2017.

[9] H. A. Madsen, T. J. Larsen, G. R. Pirrung, A. Li, and F. Zahle, "Implementation of the blade element momentum model on a polar grid and its aeroelastic load impact," *Wind Energy Science*, vol. 5, pp. 1–27, Jan. 2020.

[10] R. A. Eppler and M. Hepperle, "A Procedure for Propeller Design by Inverse Methods," 2003.

[11] S. Goldstein and L. Prandtl, "On the vortex theory of screw propellers," *Proceedings of the Royal Society of London. Series A, Containing Papers of a Mathematical and Physical Character*, vol. 123, pp. 440–465, Apr. 1929.

[12] F. Dominguez, J.-L. Achard, J. Zanette, and C. Corre, "Fast power output prediction for a single row of ducted cross-flow water turbines using a BEM-RANS approach," *Renewable Energy*, vol. 89, pp. 658–670, Apr. 2016.

[13] M. Tabib, M. S. Siddiqui, A. Rasheed, and T. Kvamsdal, "Industrial scale turbine and associated wake development -comparison of RANS based Actuator Line Vs Sliding Mesh Interface Vs Multiple Reference Frame method.," *Energy Procedia*, vol. 137, pp. 487–496, Oct. 2017.

[14] Jean-Mathieu Gagnon and Claire Deschênes, "Numerical Simulation with Flow Feature Extraction of a Propeller Turbine - Unsteady Rotor-Stator Interaction," in *Thirteenth International Conference on Computational Methods and Experimental Measurements*, 2007.

[15] J. Azinheira, "Controlo de Voo." Jan. 2009.

[16] A. Moutinho and R. J. Azinheira, "DroneX - Controlo." May 2018.